CHINA WELDING (2025) 34 (1): 28–38 https://doi.org/10.12073/j.cw.20240426027

Research Article

Effect of He-Ar shielding gas composition on the arc physical properties of laser-arc hybrid fillet welding: numerical modeling

Yaowei Wang, Wen Liu*, Peng Chen, Wenyong Zhao, Guoxiang Xu, Qingxian Hu

School of Materials Science and Engineering, Jiangsu University of Science and Technology, Zhenjiang 212003, China

Received: 26 April 2024/Accepted: 25 February 2025/Published online: 11 March 2025

Abstract

A three-dimensional numerical model of laser-arc hybrid plasma for aluminum alloy fillet joints is developed in this study. This model accounts for the geometric complexity of fillet joints, the physical properties of shielding gases with varying He-Ar ratios, and the coupling between arc plasma and laser-induced metal plume. The accuracy of the model is validated using a high-speed camera. The effects of varying He contents in the shielding gas on both the temperature and flow velocity of hybrid plasma, as well as the distribution of laser-induced metal vapor mass, were investigated separately. The maximum temperature and size of arc plasma decrease as the He volume ratio increases, the arc distribution becomes more concentrated, and its flow velocity initially decreases and then sharply increases. At high helium content, both the flow velocity of hybrid plasma and metal vapor are high, the metal vapor is concentrated on the right side of keyhole, and its flow appears chaotic. The flow state of arc plasma is most stable when the shielding gas consists of 50% He + 50% Ar.

Keywords He-Ar shielding gas components, laser-arc hybrid welding, plasma physical properties, numerical model, aluminum alloy fillet welding

1 Introduction

Laser-arc hybrid welding technology benefits from the laser-arc synergistic effect, which has the advantages of high welding speed, large weld penetration depth, good gap bridging ability, and the potential to inhibit the common weld porosity in aluminum alloys [1–2]. However, hybrid welding involves many welding parameters and a narrow process window, the process parameters are relatively difficult to optimize, and if these parameters are not properly matched, the performance of the welded joints will be easily affected [3]. The shielding gas in the welding process is crucial for the final quality of the weld. The appropriate shielding gas maintains stable arc combustion, improves welding speed, reduces welding defects, and improves weld penetration depth [4]. Therefore, an in-depth study of the effects of shielding gas composition on the arc physical properties in laser-arc hybrid welding is of great importance for improving welding stability and optimizing hybrid welding process parameters.

Research indicates that an optimal shielding gas mixture can mitigate the adverse effects of plasma on welding stability and joint quality, thus improving weld formation stability and joint mechanical properties. Li et al. [5] found that reducing the angle of shielding gas application enhances the stability of liquid metal flow in the molten pool and reduces porosity. Kuk et al. [6] discovered that increasing the helium (He) gas ratio improves the fatigue strength of arc-welded joints, with the highest strength observed at a 67% He ratio. Zhang et al. [7] reported that the corrosion resistance of MIG welded joints improves with the addition of nitrogen to the shielding gas. Lei et al. [8] investigated the effect of different shielding gases on the porosity defects in laser-welded joints of aluminum alloys. They found that the addition of He to argon (Ar) could reduce the amount of plasma, thereby improving the stability of the keyhole, and effectively controlling the porosity defects to within

* **Corresponding author:** Wen Liu, Ph. D, Mainly engaged in additive manufacturing and materials processing. E-mail: liuwen200455@126.com

1%. Similarly, Chae et al. [9] used a high-power CO_2 laser-GMAW hybrid welding method to weld shipboard steel plates and examined how different ratios of He-Ar shielding gas mixtures influenced the plasma and weld shape. The results showed that He had a superior inhibitory effect on CO_2 laser plasma. Cai et al. [10] investigated the effect of an Ar-He gas mixture on the hybrid plasma temperature, electron density, weld penetration depth, and porosity defects in laser-MIG hybrid welding by using a high-speed camera and spectral detection. They found that as the He volume ratio increased, the plasma temperature and current density decreased, while the inhibition effect of the hybrid plasma on the laser weakened. This contributed to an increase in the weld penetration depth. The stability of keyholes improved when He accounted for 50%, and the weld porosity defects were effectively suppressed. Cai et al. [11] also found that the droplet transfer modes were either short-circuited or spherical when using the He-Ar alternating shielding gas, which periodically affected the weld penetration depth. The high cost of helium and the trial-and-error experiments require a lot of resources and time. In addition, these methods do not fully elucidate the mechanism by which the shielding gas composition in fluences the arc's physical characteristics.

To address the limitations of experimental means for investigating arc physical properties, scholars have increasingly turned to numerical simulations. These simulations allow for a deeper, quantitative understanding of the plasma physical phenomena and mechanisms under various shielding gases. Rao et al. [12] established a two-dimensional numerical model of the arc and found that different He-Ar gas compositions had a significant effect on the physical properties of the arc and the transition of the molten droplets. Yang et al. [13] established a numerical analysis model of the arc and compared the effect of different shielding gas flow rates on the MIG welding and the laser-arc hybrid welding. The results show that a high shielding gas flow rate can improve the stability of the droplet transfer and the process stability of hybrid welding is higher. Wang et al. [14] developed a unified three-dimensional hybrid welding numerical model to investigate the distribution of temperature, flow velocity, and pressure of rotary laser hybrid welding plasma under different He-Ar shielding gases. However, this study only achieved a maximum He content of 50%, and the process parameter window was relatively narrow. From the above-mentioned, it is evident that there is a lack of mathematical modeling studies focused on the physical characteristics of the hybrid welding arc for aluminum alloy fillet joints under different shielding gas components. Moreover, the existing studies are not sufficient to develop a comprehensive process parameter window.

In this study, the effects of various shielding gases on the physical properties of laser-arc hybrid welding plasma for aluminum alloy fillet joints were investigated by both experimental and numerical simulations. A comprehensive three-dimensional model was developed to simulate the effects of shielding gas mixtures with varying He gas ratios on the temperature and flow velocity of arc plasma, as well as the distribution of laser-induced metal vapor mass. A high-speed camera was employed to observe the arc morphology during the welding process. By integrating experimental and simulation results, the influence mechanism of different ratios of shielding gas on the physical properties of hybrid plasma was analyzed, which is of great significance for expanding the welding process window.

2 Experimental procedures

The 6061 aluminum alloy with dimensions of 150 mm × 50 mm × 5 mm and the ER5356 with a diameter of 1.2 mm were employed as the base material and filler material, respectively. The chemical compositions of these materials are detailed in Table 1. A 6 kW continuous-wave fiber laser (IPG YLS-6000) with a wavelength of 1 075 nm, the focal length of 300 mm and the focal spot diameter of 0.3 mm was used. The MIG welding machine employed was the digital welding machine (Fronius TransPuls Synergic 4000).

Table 1 Chemical compositions of 6 061 aluminum alloy and ER5356 (wt. %)

Materials	Si	Fe	Mg	Cu	Mn	Cr	Zn	Ti	Al
6061	0.4–0.8	⩽ 0.7	0.8–1.2	0.15–0.4	0.15	0.04–0.35	0.25	⩽ 0.15	Balance
ER5356	⩽ 0.25	⩽ 0.4	4.5–5.5	⩽ 0.1	0.05–0.2	0.05–0.2	⩽ 0.1	0.06–0.2	Balance

The laser-leading welding method was employed and the laser-arc distance is 2 mm, the angles between laser and MIG welding torch are 30° and hybrid welding torch is tilted 45° relative to the horizontal plate, as shown in Fig. 1. The welding parameters used are: laser power of 3 kW, welding speed of 0.6 m/min, current of 160 A, shielding gas flow rate of 20 L/min, and welding voltage auto-matching. The shielding gas mixture

ratios are 100%Ar, 50%Ar + 50%He, and 100%He, respectively. During the welding process, a high-speed camera system (an auxiliary light source and a high-speed CP80-3-M540 camera) was used to record the arc behavior, the position of hybrid welding torch and high-speed camera was fixed, while data collection was achieved by a stepper-controlled moving welding platform.

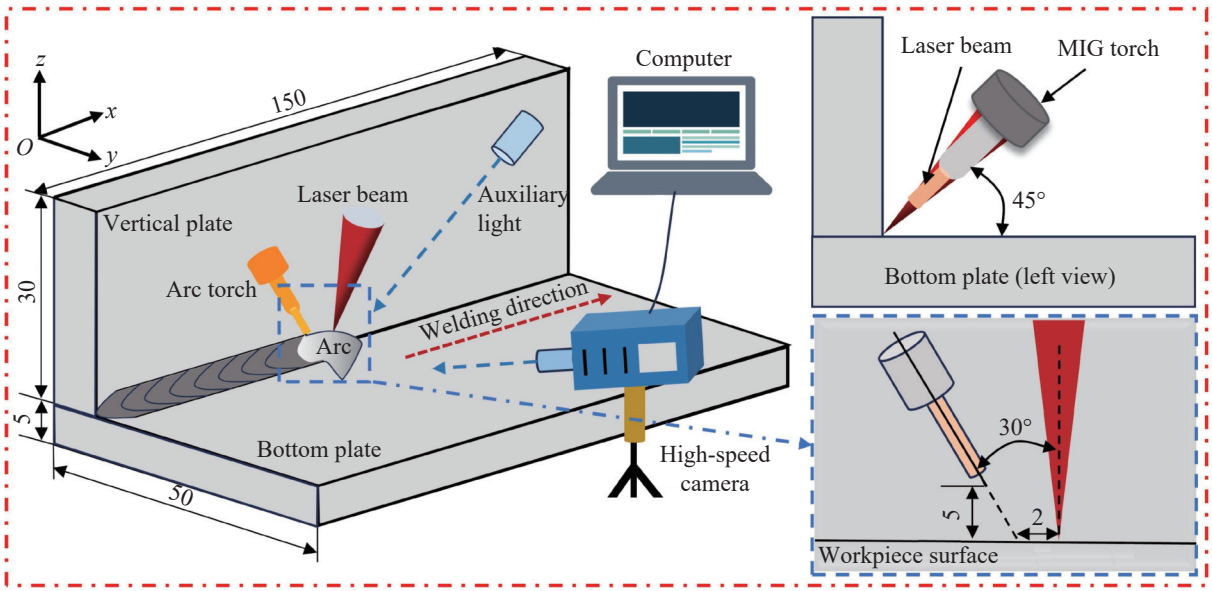

Fig. 1 **Schematic diagram of laser-MIG hybrid fillet welding system (mm)**

3 Mathematical models

3.1 Governing equations

The calculation of hybrid welding arc characteristics is extensive, due to the hybrid arc involves various physical phenomena and the coupling of laser-induced plumes (such as laser-induced plasma and metal vapor) with the arc plasma. To simplify the calculations and enhance convergence, the following simplifications are made to the model. The arc is a laminar, incompressible ideal Newtonian fluid. The high temperature metal vapor and droplets generated in the molten pool are not considered. The laser-induced plume is simplified to metal vapor ejected from a keyhole.

The governing equations for mass, momentum and energy involved in the numerical analysis are as follows, respectively [14–15]. Mass

$$\nabla\cdot(\rho v)+\frac{\partial\rho}{\partial t}=0 \tag{1}$$

where ρ denotes the density, v represents the velocity vector.

Momentum

$$\frac{\partial\rho v_i}{\partial t}+\frac{\partial}{\partial x}(\rho v v_i)=-\frac{\partial P}{\partial x}+\frac{\partial}{\partial x}\left[\left(2\mu\frac{\partial v_i}{\partial x}\right)-\frac{2}{3}\nabla\cdot v\right]+\frac{\partial}{\partial y}\left[\mu\left(\frac{\partial v_i}{\partial y}+\frac{\partial v_j}{\partial x}\right)\right]+\frac{\partial}{\partial z}\left[\mu\left(\frac{\partial v_i}{\partial z}+\frac{\partial v_k}{\partial x}\right)\right]+j_jB_k-j_kB_j \tag{2}$$

$$\frac{\partial\rho v_j}{\partial t}+\frac{\partial}{\partial y}(\rho v v_j)=-\frac{\partial P}{\partial y}+\frac{\partial}{\partial y}\left[\left(2\mu\frac{\partial v_j}{\partial y}\right)-\frac{2}{3}\nabla\cdot v\right]+\frac{\partial}{\partial z}\left[\mu\left(\frac{\partial v_j}{\partial z}+\frac{\partial v_k}{\partial y}\right)\right]+\frac{\partial}{\partial z}\left[\mu\left(\frac{\partial v_j}{\partial x}+\frac{\partial v_i}{\partial y}\right)\right]+j_kB_i-j_iB_k \tag{3}$$

$$\frac{\partial\rho v_k}{\partial t}+\frac{\partial}{\partial y}(\rho v v_k)=-\frac{\partial P}{\partial z}+\frac{\partial}{\partial z}\left[\left(2\mu\frac{\partial v_k}{\partial y}\right)-\frac{2}{3}\nabla\cdot v\right]+\frac{\partial}{\partial x}\left[\mu\left(\frac{\partial v_k}{\partial x}+\frac{\partial v_i}{\partial z}\right)\right]+\frac{\partial}{\partial y}\left[\mu\left(\frac{\partial v_k}{\partial y}+\frac{\partial v_j}{\partial z}\right)\right]+j_iB_j-j_jB_i \tag{4}$$

where v_i, v_j and v_k are the velocity vectors along the x, y, and z axes, respectively; P denotes the pressure; μ is the viscosity coefficient; j_i, j_j and j_k denote the current density components in the three directions and B_i, B_j and B_k

indicate the induced magnetic field intensity components along the three axes, respectively.

Energy

$$\frac{\partial \rho h_e}{\partial t} + \nabla \cdot (\rho v h_e) = \nabla \cdot \left(\frac{k}{c_p} \nabla h_e \right) + \frac{{j_x}^2 + {j_y}^2 + {j_z}^2}{\sigma_e} - 4\pi\zeta + \frac{5k_B}{2e} j \cdot \nabla T + Q_{laser} \tag{5}$$

where h_e represents the enthalpy; c_p, σ_e, k_B, ζ are the specific heat capacity, electrical conductivity, Boltzmann constant and net radiation coefficient associated with the material, respectively. On the right side of the equation, the second, third, and fourth terms denote the Joule heat, heat lost to the outside, and heat of electron migration, respectively; Q denotes the lost laser energy.

Electromagnetic field equation

Current continuity equation

$$\frac{\partial}{\partial x}\left(\sigma_e \frac{\partial \phi}{\partial x}\right) + \frac{\partial}{\partial y}\left(\sigma_e \frac{\partial \phi}{\partial y}\right) + \frac{\partial}{\partial z}\left(\sigma_e \frac{\partial \phi}{\partial z}\right) = 0 \tag{6}$$

Current density component

$$\begin{cases} j_x = -\sigma_e \dfrac{\partial \phi}{\partial x} \\ j_y = -\sigma_e \dfrac{\partial \phi}{\partial y} \\ j_z = -\sigma_e \dfrac{\partial \phi}{\partial z} \end{cases} \tag{7}$$

where ϕ is the electric potential.

Magnetic field components

$$\frac{\partial^2 A_i}{\partial x^2} + \frac{\partial^2 A_i}{\partial y^2} + \frac{\partial^2 A_i}{\partial z^2} = -\mu_0 j_i \tag{8}$$

$$\frac{\partial^2 A_j}{\partial y^2} + \frac{\partial^2 A_j}{\partial x^2} + \frac{\partial^2 A_j}{\partial z^2} = -\mu_0 j_j \tag{9}$$

$$\frac{\partial^2 A_k}{\partial z^2} + \frac{\partial^2 A_k}{\partial y^2} + \frac{\partial^2 A_k}{\partial x^2} = -\mu_0 j_k \tag{10}$$

$$\begin{cases} B_i = \dfrac{\partial A_k}{\partial y} - \dfrac{\partial A_j}{\partial z} \\ B_j = \dfrac{\partial A_i}{\partial z} - \dfrac{\partial A_k}{\partial x} \\ B_k = \dfrac{\partial A_j}{\partial x} - \dfrac{\partial A_i}{\partial y} \end{cases} \tag{11}$$

where A_i, A_j and A_k are the magnetic vector components along the x, y and z axes, respectively; μ_0 is the vacuum permeability.

Metal vapor transport equation

$$\frac{\partial}{\partial t}(\rho f_v) + \nabla \cdot (\rho v f_v) = \nabla \cdot (\rho D \nabla f_v) \tag{12}$$

where f_v is the mass fraction of metal vapor and D is the diffusion coefficient, calculated using the viscosity approximation equation.

$$D = \frac{2\sqrt{2}\left(\dfrac{1}{m_1} + \dfrac{1}{m_2}\right)^{\frac{1}{2}}}{\left\{\left({\rho_1}^2/{\beta_1}^2{\eta_1}^2 m_1\right)^{\frac{1}{4}} + \left({\rho_2}^2/{\beta_2}^2{\eta_2}^2 m_2\right)^{\frac{1}{4}}\right\}^2} \tag{13}$$

where m_1 and m_2 denote the molar masses of aluminum and mixed shielding gases, respectively; ρ_1, ρ_2, η_1, and η_2 represent the densities and viscosity of aluminum metal vapor and shielding gases, respectively; β_1 and β_2 are dimensionless constants. For gases such as Ar, He, H_2, N_2, O_2 and CO_2, β_1 and β_2 are theoretically in the range of 1.2 to 1.543 [16], this paper assumes $\beta_1 = \beta_2 = 1.3$ [17].

3.2 Metal vapor model

The metal vapor plasma is assumed to be ejected at high velocity from the keyhole and described its generation using the component transport equation. The parameters of the high-speed ejection of laser-induced plasma at the keyhole, such as temperature and velocity, are referenced from the relevant model established by Dilthey et al. [18]. This model elucidates the dynamic interplay among the keyhole radius, plasma temperature, and laser energy density highlighting their mutual dependencies. The relationship between the temperature of the laser-induced plasma and the laser energy density is expressed as follows:

$$\begin{aligned} T &= 0.004\,25I + 3\,240.384\,62, \quad 0.20\ \text{mm} < R \leqslant 0.30\ \text{mm} \\ T &= 0.004\,31I + 3\,252.136\,75, \quad 0.30\ \text{mm} < R \leqslant 0.40\ \text{mm} \\ T &= 0.004\,38I + 3\,263.888\,89, \quad 0.40\ \text{mm} < R \leqslant 0.50\ \text{mm} \end{aligned} \tag{14}$$

where T is the plasma temperature, I is laser energy density, R is the keyhole radius.

The ejection velocity of metal vapor is determined according to the laser keyhole surface metal vapor flow model established by Amara et al. [19]. The formula is as follows:

$$V_g = \sqrt{\kappa \frac{LT_k}{m_a}} \tag{15}$$

where κ is the specific heat capacity, L is the ideal gas constant, T_k is the temperature at the keyhole surface, and m_a is the atomic mass.

3.3 Boundary conditions

The model boundary conditions are shown in Fig. 2a. The welding wire tip is designated as the anode, while its remaining surfaces are defined as the wall. The upper surface of the model is designated as the inlet for shielding gas and the lower surface of the workpiece is assigned as the cathode. The keyhole region is configured as the velocity inlet for laser-induced metal vapor eruption, and the remaining boundaries are set as pressure outlet. The length of calculation area along the welding direction is 25 mm, the model height is 7 mm, the initial arc length is 5 mm, and the laser arc distance is 2 mm, as displayed in Fig. 2b. In this study, a non-uniform mesh was used to discretize the model, employing a finer grid with a minimum mesh size of 0.2 mm in areas around the weld wire and the laser-induced metal vapor eruption. Conversely, a coarser grid with a maximum mesh size of 0.3 mm was applied to the remaining regions. Additionally, a variable time step strategy was adopted, with a minimum time step of 10^{-6} s. The high-temperature thermal physical properties of metallic aluminum vapor, argon gas, and helium gas were referenced from [20]. For the physical properties of helium-argon mixtures and aluminum metal vapors, values were interpolated linearly as described in references [21–23].

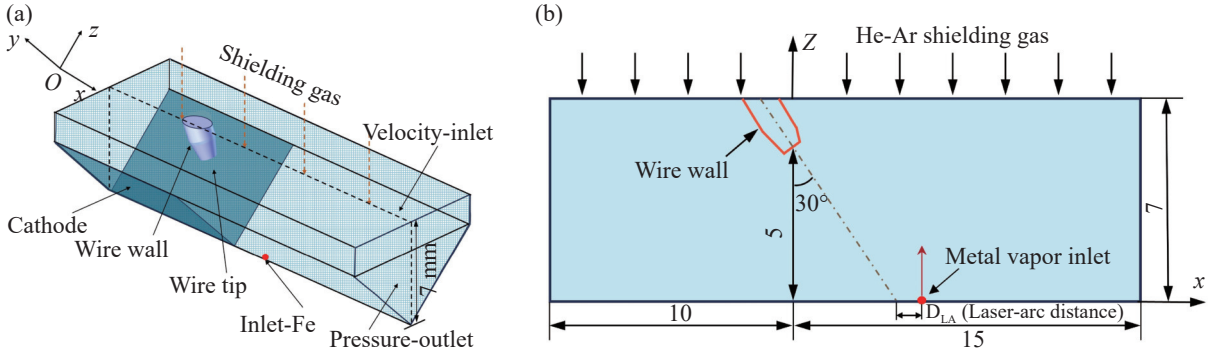

Fig. 2 Schematic diagram of model: (a) boundary conditions, (b) calculation domain (mm)

4 Results and discussion

To analyze the physical properties of arc plasma more clearly, different cross-sections are selected as illustrated in Fig. 3. Specifically, cross-section 1 and cross-section 2 represent the locations of the welding wire and the laser-induced metal vapor, respectively.

4.1 Arc temperature

Since the peak temperature of the arc plasma varies with shielding gas composition, and its distribution becomes localized near the electrode tip when exceeding 16 000 K, the color scale for temperature in all figures is set to a range of 2 000 K–16 000 K to enhance the contrast in arc distribution characteristics. The same range is applied to the color scale of the arc plasma velocity field throughout subsequent sections. Fig. 4 shows the distributions of arc plasma temperature field in the transverse and longitudinal section by various shielding gas compositions. It is observed that the hybrid shield-

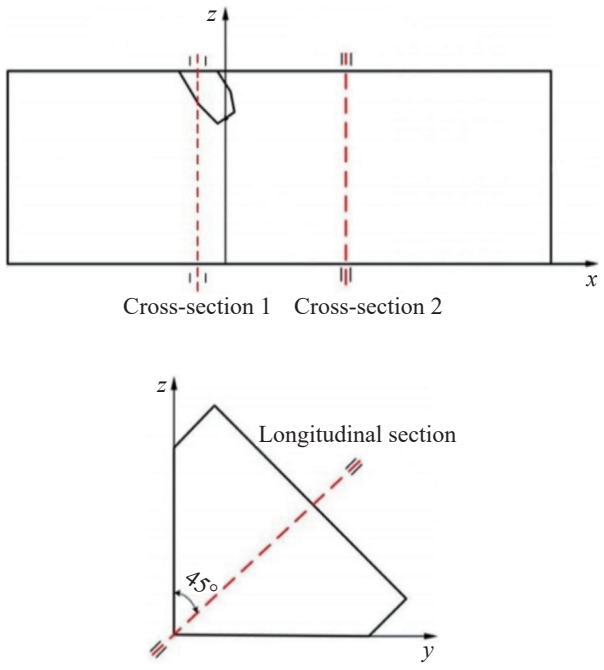

Fig. 3 Schematic representation of selected transverse and longitudinal sections

ing gases with different He contents have a significant effect on the temperature distribution of the arc plasma. In the longitudinal section, the temperature distribution range of hybrid plasma decreases as the He content increases. When the He content reaches 100%, the distribution length of the hybrid plasma in the x-direction is 12 mm, compared to 24 mm for pure Ar. With He and Ar both at 50% in the shielding gas, the size of the hybrid plasma on the electrode's left side decreases significantly. As the He volume fraction increases to 100%, the overall size of the arc plasma reduces to half of its initial size, as shown in Fig. 4(a1–c1). Meanwhile, the maximum temperature of the hybrid plasma decreases significantly to 25 088.9 K, 20 970.2 K, and 18 493 K. Initially, the peak temperature of the plasma decreases substantially, but the rate of decrease slows down over time. Similar variations in arc temperature have been observed in references [10, 14], which indirectly supports the validity of the developed model.

In cross-section, the arc plasma is symmetrically distributed along the electrode direction. Due to the limitations of the cross-sectional size, the overall dimensions of the hybrid plasma remain relatively constant. However, the temperature variation pattern is consistent with that observed in the longitudinal section, decreasing from 25 068.9 K to 20 702.2 K and then to

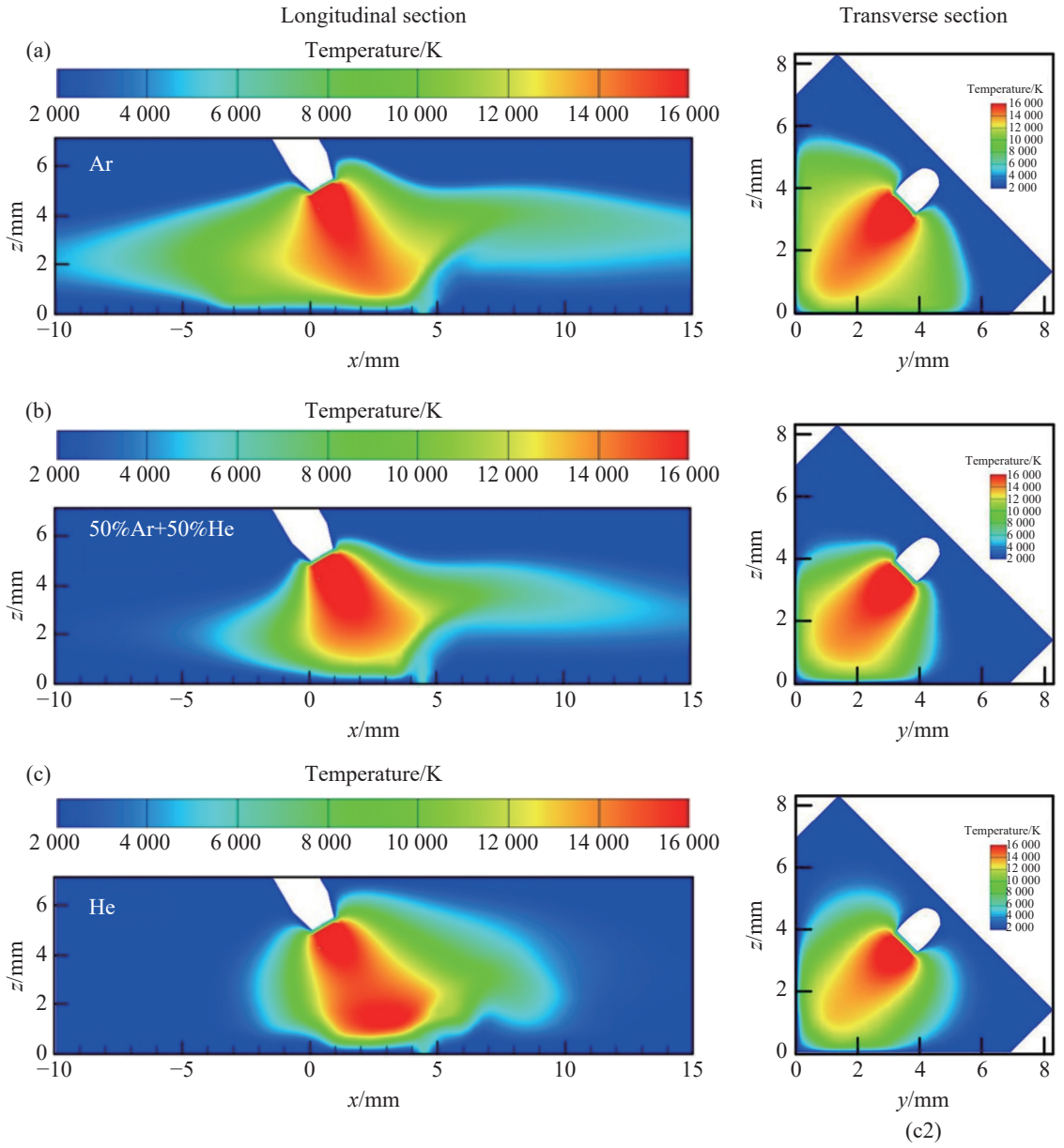

Fig. 4 Arc temperature distributions in the transverse and longitudinal section for various shielding gas: (a) 100%Ar; (b) 50%He + 50%Ar; (c) 100%He

18 237.5 K, respectively. Compared to pure argon gas, He gas has higher ionization energy and thermal conductivity, resulting in a smaller plasma size and lower temperature. Previous literature [10, 24–25] indicates that the shielding effect of plasma generated by a He-Ar mixed shielding gas on the laser is weakened. Therefore, He-Ar mixed shielding gas is beneficial for improving weld penetration depth.

4.2 Plasma velocity

Fig. 5 shows the distribution of arc plasma velocity in the cross section and longitudinal section under different shielding gas proportions. The arc plasma flows at high speed along the electrode direction. After reaching the workpiece surface, most of it flows to the right along the positive x direction. At the keyhole, it intersects with the laser-induced metal plume and subsequently deflects upward and to the right. Unlike the temperature trend of the plasma, its flow velocity first decreases and then sharply increases with an increasing He volume ratio, and its flow velocities are 319.3 m/s, 265.3 m/s and 893 m/s, respectively. When the He content is 100%, the flow morphology of the arc plasma is significantly affected by the laser-induced metal plume, as shown in Fig. 5(c1). Additionally, cross-sectional observations reveal that the arc plasma is no longer symmetrically dis-

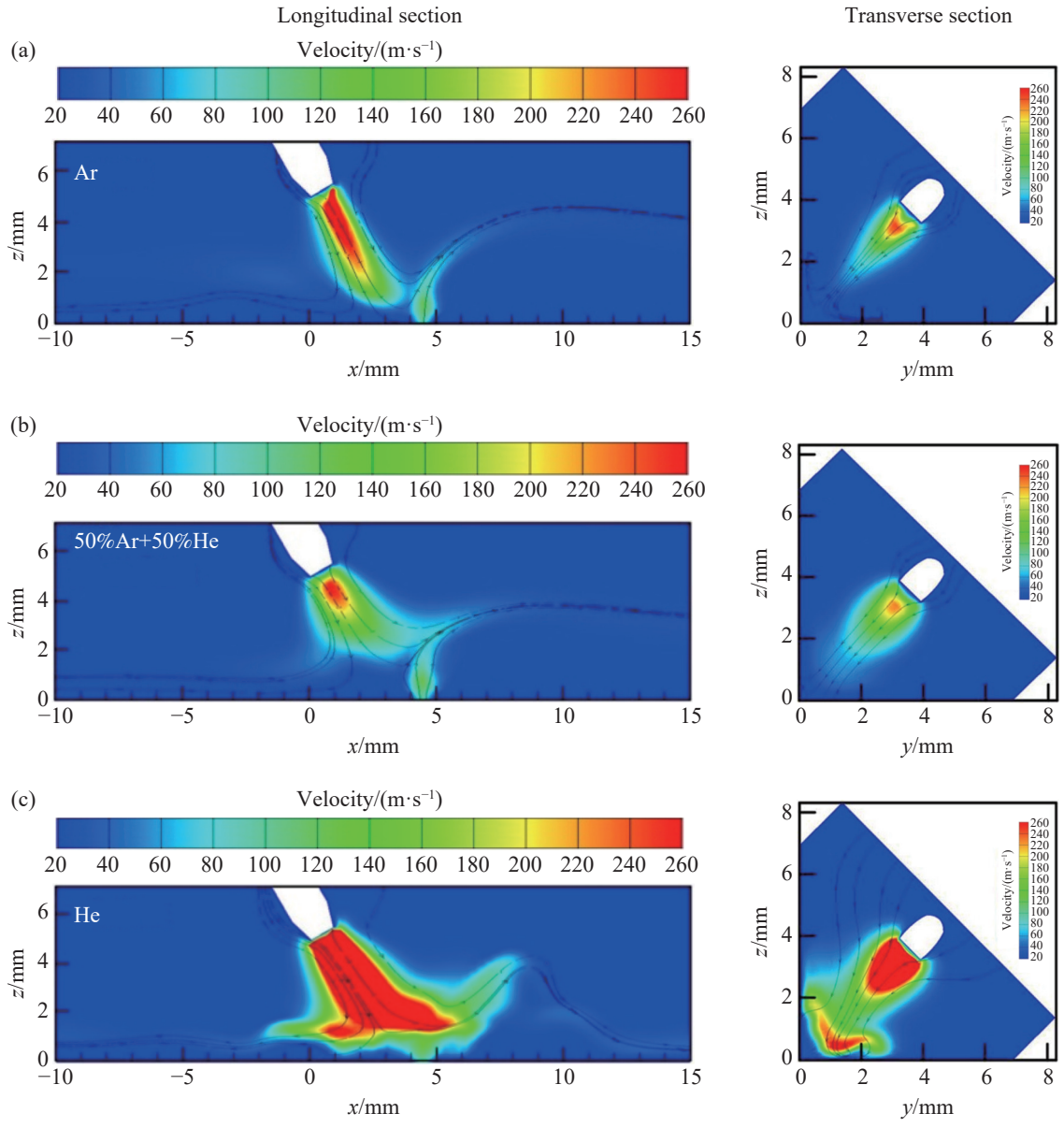

Fig. 5 Hybrid plasma velocity in the transverse and longitudinal section for various shielding gas: (a) 100%Ar, (b) 50%He + 50%Ar, (c) 100%He

tributed along the electrode, which may adversely affect weld formation.

Fig. 6 shows the distributions of laser-induced metal vapor in the transverse and longitudinal section under different shielding gas proportions. It is observed that, the maximum aluminum metal vapor mass fraction is observed near the keyhole on the workpiece surface, aluminum metal vapor is ejected upward from the keyhole at a high speed, and deflected to the right after meeting the arc plasma during movement. When using pure Ar and 50% He + 50% Ar, the distribution of metal vapor remains stable, and its eruption height is slightly reduced. When pure He is used, the metal distribution state becomes complex and chaotic, depicted in Fig. 6c, and the plasma is even more biased to the vertical plate side, which undermines the stability of the hybrid plasma. Based on the analysis, the gas Ar has a good effect of arc initiation and stabilization [12, 26]. However, increasing helium content in the shielding gas while reducing argon content can inhibit arc stability. Although helium can enhance weld penetration depth, excessively high helium levels are detrimental to arc stability [10].

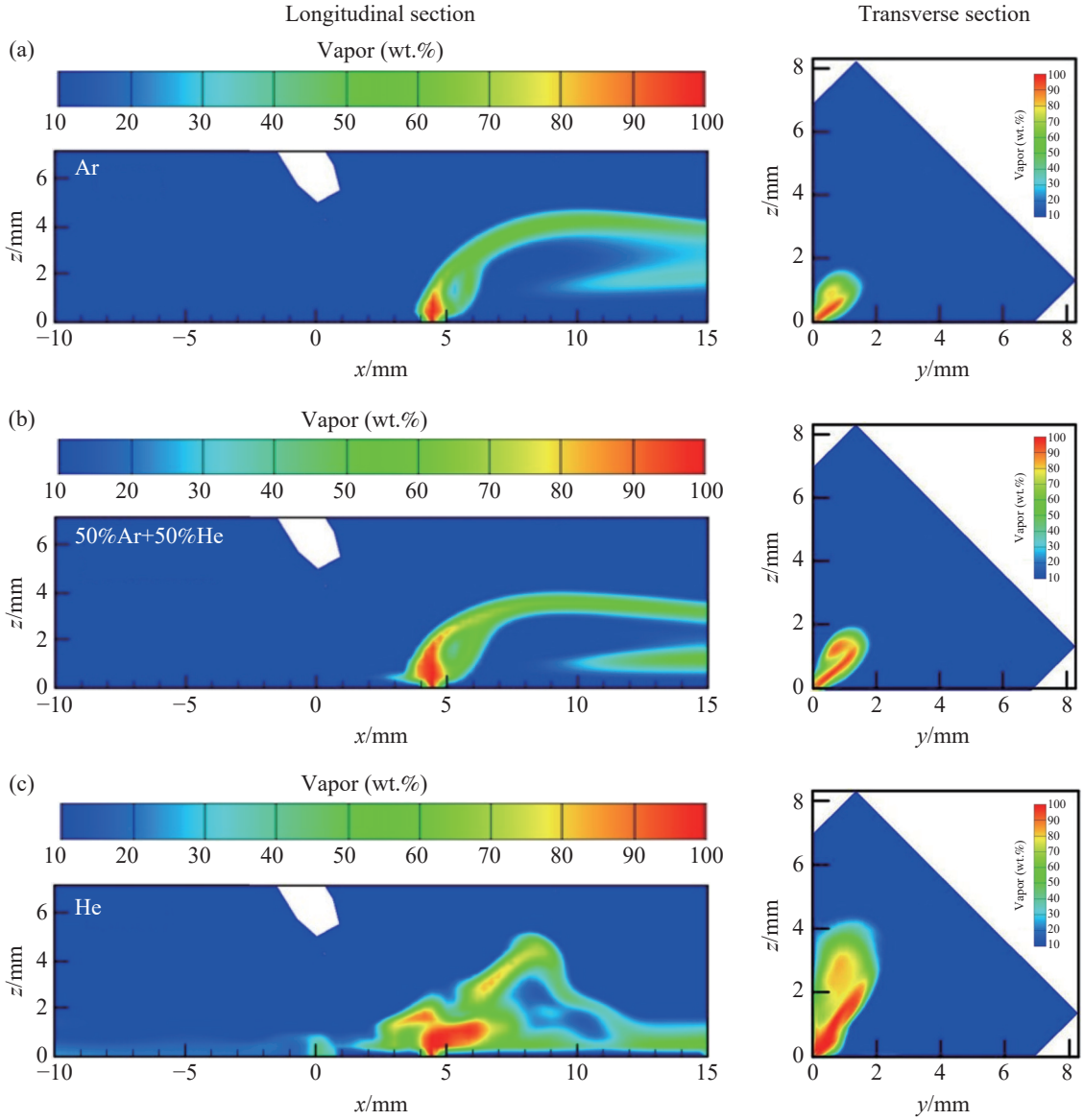

Fig. 6 Metal vapor in the transverse and longitudinal section for various shielding gas: (a) 100%Ar, (b) 50%He + 50%Ar, (c) 100%He

4.3 Verification of model

Fig. 7 and Fig. 8 compare the calculated arc plasma morphology and size with measured data for various shielding gas compositions. The results show that the plasma

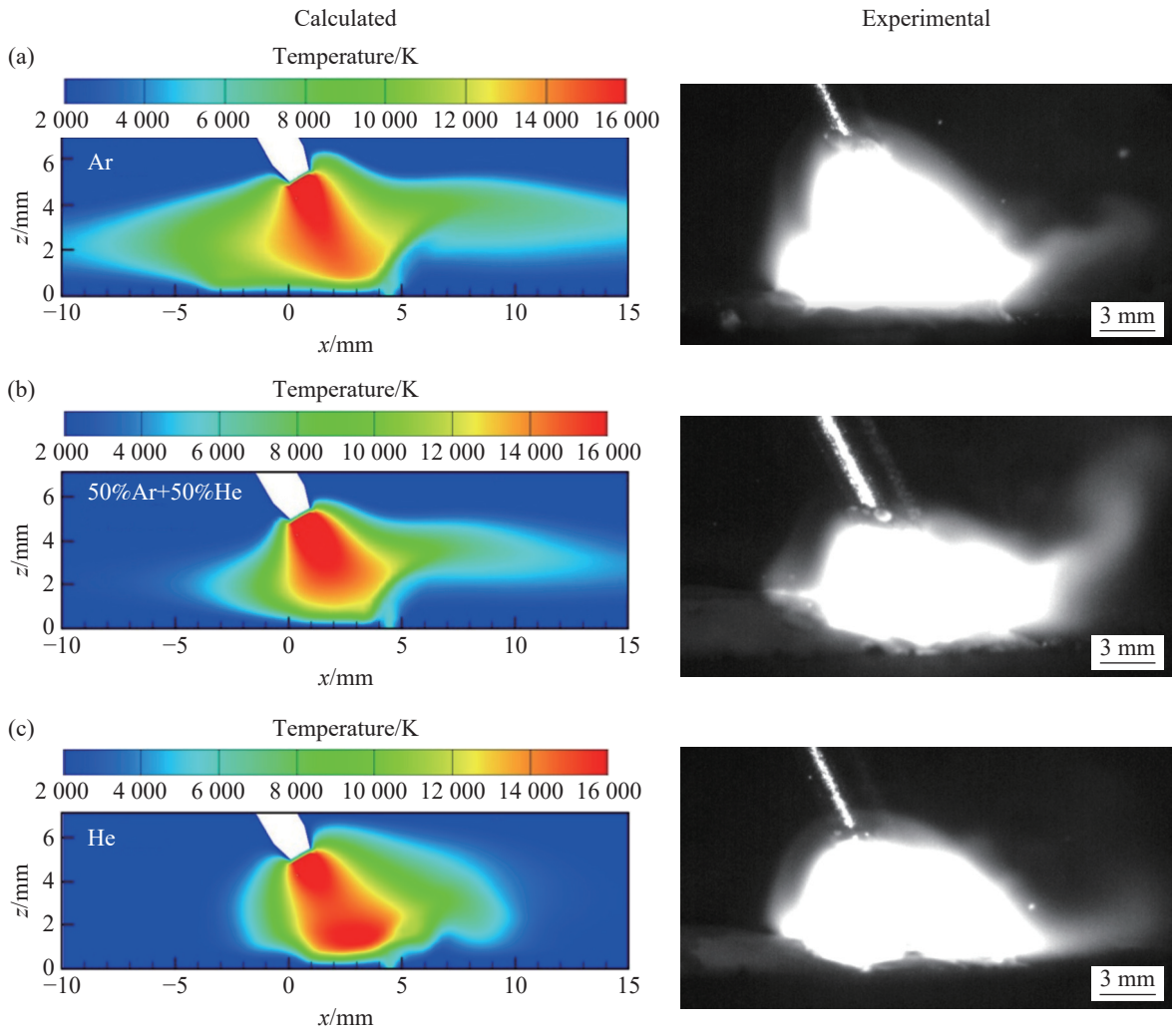

Fig. 7 Comparison of experimental detection and calculation results of arc plasma morphology: (a) 100%Ar, (b) 50%He + 50%Ar, (c) 100%He

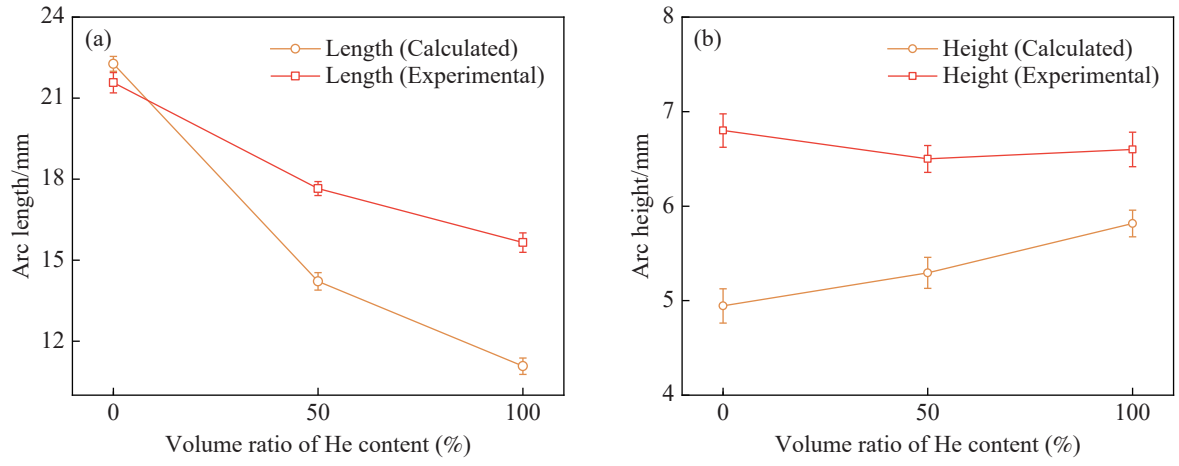

Fig. 8 Comparison of calculated arc plasma sizes with experimental data: (a) Arc length, (b) Arc height

shapes obtained from simulation and experiment are basically consistent, indicating that the established model can accurately reflect the physical properties of hybrid arc plasma under different shielding gas compositions.

The arc in the actual welding process is influenced by various external factors, and the established model simplifies some of these physical interactions. Additionally, the model does not fully incorporate the high-temperature properties of materials and shielding gases, resulting in a certain degree of discrepancy between experimental and computational results. Our research team is committed to further studies to reduce these errors.

5 Conclusion

(1) A comprehensive three-dimensional model has been developed, accounting for the geometric complexity of filled joints, the physical properties of various shielding gas components, and the coupling of the arc plasma and laser-induced plume. The model analyzes the temperature and velocity distribution of the hybrid plasma under different shielding gas conditions. Its accuracy is validated by comparing the calculated results with experimental data.

(2) With the increase of shielding gas He content, the arc distribution becomes more concentrated, the size and maximum temperature of the hybrid plasma decreases, and its inhibition effect on the laser is weakened, which is conducive to improving the weld penetration. The flow rate of the hybrid plasma initially decreases but then rises sharply. Under pure helium, the metal vapor is concentrated on the right side of keyhole and its flow appears chaotic, and the plasma is more stable when the shielding gas is 50% He + 50% Ar.

Acknowledgments

This work is financially supported by the National Natural Science Foundation of China (Grant No.52375340, 51975263, 52405366).

Author contributions

Yaowei Wang: Writing–original draft, software, formal analysis, data curation, conceptualization. Wen Liu : Investigation, project administration, funding acquisition. Peng Chen : Data curation, software. Wenyong Zhao: Writing – review & editing, software. Guoxiang Xu: Conceptualization, supervision, project administration, funding acquisition, writing–review & editing. Qingxian Hu: Conceptualization, supervision, formal analysis.

Conflict of interest

The authors declare that they have no conflict of interests.

References

[1] Acherjee B. Hybrid laser arc welding: State-of-art review. Optics & Laser Technology 2018, 99: 60–71. https://doi.org/10.1016/j.optlastec.2017.09.038

[2] Bagger C, Olsen FO. Review of laser hybrid welding. Journal of Laser Applications, 2005, 17:2–14. https://doi.org/10.2351/1.1848532

[3] Xu G X, Li L, Wang H, et al. Simulation and experimental studies of keyhole induced porosity in laser-MIG hybrid fillet welding of aluminum alloy in the horizontal position. Optics & Laser Technology, 2019, 119:105667. https://doi.org/10.1016/j.optlastec.2019.105667

[4] Tani G, Campana G, Fortunato A, et al. The influence of shielding gas in hybrid LASER–MIG welding. Applied Surface Science, 2007, 253(19):8050–8053. https://doi.org/10.1016/j.apsusc.2007.02.144

[5] Li K, Lu F, Cui H, et al. Investigation on the effects of shielding gas on porosity in fiber laser welding of T-joint steels. The International Journal of Advanced Manufacturing Technology, 2015, 77:1881–1888. https://doi.org/10.1007/s00170-014-6538-4

[6] Kuk J M, Jang K C, Lee D G, et al. Effects of temperature and shielding gas mixture on fatigue life of 5083 aluminum alloy. Journal of Materials Processing Technology, 2004, 155–156: 1408–1414. https://doi.org/10.1016/j.jmatprotec.2004.04.117

[7] Zhang X Y, Zha X Q, Gao L Q, et al. Influence of shielding gas on microstructure and properties of GMAW DSS2205 welded joints. Materials, 2021, 14(10):2671. https://doi.org/10.3390/ma14102671

[8] Lei Z, Li Y, Chen Y, et al. Effect of process parameters on porosity formation ratio in dual-beam laser welding of aluminum alloys with filler wire. Transactions of the China Welding Institution, 2013, 34(2):40–44. (in Chinese)

[9] Chae H B, Kim C H, Kim J H, et al. The effect of shielding gas composition in CO_2 laser —gas metal arc hybrid welding. Proceedings of the Institution of Mechanical Engineers, Part B: Journal of Engineering Manufacture, 2008, 222(11):1315–1324. https://doi.org/10.1243/09544054JEM944

[10] Cai C, He S, Chen H, et al. The influences of Ar-He shielding gas mixture on welding characteristics of fiber laser-MIG hybrid welding of aluminum alloy. Optics & Laser Technology, 2019, 113:37–45.

[11] Cai X, Fan C, Lin S, et al. Effects of shielding gas composition on arc behaviors and weld formation in narrow gap tandem GMAW. The International Journal of Advanced Manufacturing Technology, 2017, 91:3449–3456. https://doi.org/10.1007/s00170-017-9990-0

[12] Rao Z H, Liao S M, Tsai H L. Effects of shielding gas compositions on arc plasma and metal transfer in gas metal arc welding. Journal of applied physics, 2010, 107(4): 044902. https://doi.org/10.1063/1.3291121

[13] Yang X, Chen H, Zhu Z, et al. Effect of shielding gas flow on welding process of laser-arc hybrid welding and MIG welding. Journal of Manufacturing Processes, 2019, 38:530–542. https://doi.org/10.1016/j.jmapro.2019.01.045

[14] Wang Y W, Liu W, Li W D, et al. Effects of He-Ar shielding gas compositions on arc plasma physical properties in rotating laser + GMAW hybrid fillet welding: Numerical simulation. Optics & Laser Technology, 2024, 178:111231. https://doi.org/10.1016/j.optlastec.2024.111231

[15] Xu G, Zheng Z, Cao Q, et al. Numerical and experimental investigation on weld formation during laser + MIG hybrid fillet welding of aluminum alloy in horizontal position. The International Journal of Advanced Manufacturing Technology, 2019, 102:2683–2694. https://doi.org/10.1007/s00170-019-03372-3

[16] Tanaka M, Yamamoto K, Tashiro S, et al. Time-dependent calculations of molten pool formation and thermal plasma with metal vapour in gas tungsten arc welding. Journal of Physics D: Applied Physics, 2010, 43(43):434009. https://doi.org/10.1088/0022-3727/43/43/434009

[17] Wilke C R. A viscosity equation for gas mixtures. The Journal of Chemical Physics, 1950, 18(4):517–519. https://doi.org/10.1063/1.1747673

[18] Dilthey U, Goumeniouk A, Lopota V A. Kinetic description of keyhole plasma in laser welding. Journal of Physics D, Applied Physics, 2000, 33: 2747–2753.

[19] Amara E H, Fabbro R, Bendib A. Modeling of the compressible vapor flow induced in a keyhole during laser welding. Journal of Applied Physics, 2003, 93:4289–4296. https://doi.org/10.1063/1.1557778

[20] Murphy A B. The effects of metal vapour in arc welding. Journal of Physics D: Applied Physics, 2010, 43(43):434001. https://doi.org/10.1088/0022-3727/43/43/434001

[21] Schnick M, Fuessel U, Hertel M, et al. Modelling of gas metal arc welding taking into account metal vapour. Journal of Physics D: Applied Physics, 2010, 43(43): 434008. https://doi.org/10.1088/0022-3727/43/43/434001

[22] Essoltani A, Proulx P, Boulos M I, et al. Volumetric emission of argon plasmas in the presence of vapors of Fe, Si, and Al. Plasma Chemistry and Plasma Processing, 1994, 14:437–450. https://doi.org/10.1007/BF01570206

[23] Gleizes A, Cressault Y, Teulet P. Mixing rules for thermal plasma properties in mixtures of argon, air and metallic vapours. Plasma Sources Science and Technology, 2010, 19(5):055013. https://doi.org/10.1088/0963-0252/19/5/055013

[24] Cai C, Peng G C, Li L Q, et al. Comparative study on laser welding characteristics of aluminium alloy under atmospheric and subatmospheric pressures. Science and Technology of Welding and Joining, 2014, 19(7):547–553. https://doi.org/10.1179/1362171814Y.0000000223

[25] Menzel M. The influence of individual components of an industrial gas mixture on the welding process and the properties of welded joints. Welding International, 2003, 17(4):262–264. https://doi.org/10.1533/wint.2003.3111

[26] Beck M, Berger P, Hugel H. The effect of plasma formation on beam focusing in deep penetration welding with CO_2 lasers. Journal of Physics D: Applied Physics, 1995, 28(12):2430. https://doi.org/10.1088/0022-3727/28/12/007